Selective control over the morphology and the oxidation state of iron oxide nanoparticles

Mariona Escoda-Torroella,[1,2] Carlos Moya,[1-3]* Arantxa Fraile Rodríguez,[1,2] Xavier Batlle,[1,2] and Amílcar Labarta,[1,2]

[1]Departament de Física de la Matèria Condensada, Martí i Franquès 1, 08028 Barcelona, Spain
[2]Institut de Nanociència i Nanotecnologia, Universitat de Barcelona, 08028 Barcelona, Spain
[3]Université libre de Bruxelles (ULB), Engineering of Molecular Nanosystems, 50 Avenue F.D. Roosevelt, 1050 Bruxelles, Belgium

ABSTRACT Iron oxide nanoparticles (NPs) have been extensively used for both health and technological applications. The control over their morphology, crystal microstructure and oxidation state are of great importance to optimize their final use. However, while mature in understanding, it is still far from complete. Here we report on the effect of the amount of either 1,2-hexadecanediol and/or 1-octadecene in the reaction mixture on the thermal decomposition of iron (III) acetylacetonate in oleic acid for two series of iron oxide NPs with sizes ranging from 6 to 48 nm. We show that a low amount of either compound leads to both large, mixed-phase NPs composed of magnetite (Fe_3O_4) and wüstite (FeO) and high reaction yields. In contrast, a higher

amount of either 1,2-hexadecanediol or 1-octadecene gives rise to smaller, single-phase NPs with moderate reaction yields. By infrared spectroscopy, we have elucidated the role of 1,2-hexadecanediol, which mediates in the particle nucleation and growth. Finally, we have correlated the magnetic response and the structural features of the NPs for the two series of samples

Introduction

Magnetic nanoparticles (NPs) have been largely investigated in the last decades because of their current and potential applications in storage media,[1–3] environmental remediation,[4] and biomedicine.[5–9] In particular, iron oxide NPs composed of magnetite (Fe_3O_4) and/or maghemite (γ-Fe_2O_3) have been extensively employed with medical purposes because of their fascinating chemical and physical features. To name a few, their easy functionalization, low toxicity and good magnetic properties make them excellent candidates for magnetic recoverable catalysts,[4,10] biosensing,[5,11–13] drug delivery,[14–16] and as contrast agents for magnetic resonance imaging,[17–20] among others. Besides, the low price of the iron reagents enables the production of large amounts of NPs with low costs of production. From the fundamental point of view, iron oxide NPs are also ideal candidates to study fundamental phenomena because of the emergence of new or enhanced properties as compared with the bulk counterpart; for example, the appearance of superparamagnetic behavior, the increase of the magnetic anisotropy, both the reduction or the improvement of the magnetic response, and the vanishing of the Verwey transition in Fe_3O_4 NPs.[9,21–25]

The thermal decomposition of iron acetylacetonate ($Fe(acac)_3$) in presence of fatty acids stands out among the common synthesis methods to obtain iron-oxide NPs because it allows a very precise control over particle size and shape.[26,27] However, there are still some issues to be addressed regarding the control over the particle composition depending on the solvent employed

in the reaction mixture. 1-octadecene is one of the most used solvents in the preparation of NPs because of two reasons. Firstly, it enables a very good tuning of the particle size distribution, since its high boiling point ensures a nucleation temperature separated enough from the precursor decomposition temperature. Secondly, its low reactivity inhibits secondary reactions; thus, favoring the formation of a great number of particles. However, the main drawback of this solvent is its weaker antioxidant behavior that inhibits the thermal decomposition of $Fe(acac)_3$.[28] As a result, nucleation and growth processes are hampered and the reaction is delayed. In this context, secondary phases energetically stable can appear within the particle structure. The most common case is the presence of wüstite (FeO) crystallites as a secondary phase within the Fe_3O_4 NPs.[29–32] Note that FeO dissociates to Fe_3O_4 and Fe below 560 ºC but can be metastable at the nanoscale.[33] Besides, FeO is antiferromagnetic (AFM) below 198 K. Consequently, particles enriched with this phase show a dramatic change in their magnetic properties compared to the homogeneous single-phase Fe_3O_4 counterparts, namely a higher magnetic anisotropy, a strong reduction of the saturation magnetization and the presence of a horizontal shift of the hysteresis loop after a field cooling procedure (i.e., exchange bias). Furthermore, 1,2-hexadecanediol has been extensively employed to ensure a controlled reduction of reagents. Nevertheless, the effect of its concentration in the reaction mixture on the precise morphology, oxidation state and magnetic response of iron oxide NPs is not well understood yet.

Within this framework, we report on the results of the synthesis of two series of iron oxide NPs by the rational monitoring of the effects of the amounts of either 1,2-hexadecanediol and 1-octadecene on the thermal decomposition of $Fe(acac)_3$ in the presence of oleic acid. We have tuned the amounts in the reaction mixture of both 1,2-hexadecanediol and 1-octadecene from 0 to 12 mmol and 0 to 20 mL, respectively. Next, we have evaluated the effect of each reagent on the

structural parameters, such as size, particle shape and composition, and reaction yield (η). We have also gained insight into the role of each reagent on the reaction mechanism by an infrared study of aliquots at different reaction stages. To finish, we have correlated the magnetic behavior of their samples to their structural features.

Experimental Section

Materials. Iron (III) acetylacetonate (Fe(acac)$_3$, 99.9%), 1,2-hexadecanediol (90%), oleic acid (90%), 1-octadecene (90%) were purchased from Sigma-Aldrich. Nitric acid (HNO$_3$, 65%), acetone (99,9%) and hexane (95%) were bought from Panreac. All materials were used as received without further purification.

Synthesis of oleic acid coated iron oxide NPs. The effect of the stabilizer reagent (1,2-hexadecanediol) and the solvent (1-octadecene) were evaluated in the synthesis of 7 nm NPs following a standard procedure described elsewhere.[27,34] First, 0.36 g of Fe(acac)$_3$ (1 mmol), 1.15 g of oleic acid (4 mmol) and 1.5 g of 1,2-hexadecanediol (6 mmol) were mixed with 5 mL of 1-octadecene at 1100 rpm using a Teflon coated magnetic stir bar in a three-neck flask. The reaction mixture was purged at 105 °C for 30 min under low pressure, and then the reaction temperature was increased at 3.2 °C/min up to 200 °C and kept at this temperature for two hours under argon flow. Afterwards, the temperature was raised at 11 °C/min up to 310 °C and kept constant for one hour. Then, the heating mantle was removed, and the reaction mixture was cooled down until room temperature. After, it was mixed with 60 mL of hexane and acetone mixture, with a ratio of 1:3, transferred to two 50 mL centrifuge tubes, and centrifuged at 9000 rpm for ten minutes. The black precipitate of each tube was dispersed with 40 mL of the mixture of hexane and acetone and washed by centrifugation a minimum of three times. Finally, the precipitate was dried using

compressed nitrogen gas for 30 seconds, dispersed in 5 mL of hexane, and stored at 5 ºC. This sample was labelled as S7.

After that, two series of samples were prepared varying the amount of either 1,2-hexadecanediol or 1-octadecene in the reaction mixture. To simplify the reading, hereafter the samples obtained with tunable amounts of 1,2-hexadecanediol or 1-octadecene will be labelled as S_{OH} and S_{OC}, respectively. Firstly, three samples were prepared changing only the amount of 1,2-hexadecanediol in the reaction mixture as follows: 12, 2.5 and 0 mmol, referred to as $S_{OH}6$, $S_{OH}10$, and $S_{OH}16$, respectively. Secondly, three additional samples were prepared modifying only the amount of 1-octadecene in the reaction mixture as indicated: 20, 2.5 and 0 mL, referred to as $S_{OC}6$, $S_{OC}29$ and $S_{OC}48$, respectively.

Characterization

Transmission electron microscopy (TEM). The morphology and size of the NPs in the samples were determined using a JEOL 1010 microscope operating at 100 kV. TEM samples were prepared by placing a drop of a diluted suspension of NPs in hexane onto a carbon-coated Cu grid and letting it dry for 10 minutes at 90 ºC. Particle histograms were determined analyzing at least 500 particles with the Image J software.[35] The resulting histograms of the particle diameters D were fitted to a log-normal distribution of the form

$$P(D) = \frac{1}{S\sqrt{2\pi}D} e^{-\ln^2\left(\frac{D}{D_0}\right)/(2S^2)} \tag{1}$$

except those from sample $S_{OC}16$ (see Figure S1 from Supporting Information) and $S_{OC}29$, which were fitted to the superposition of two log-normal functions since these samples showed clear particle bimodality. The mean particle size, D_{TEM}, and the standard deviation σ were computed from eq 2 and 3, respectively,

$$D_{TEM} = D_0 e^{S^2/2} \tag{2}$$

$$\sigma = D_0 e^{S^2/2} \sqrt{e^{S^2} - 1} \qquad (3)$$

where D_0 and S are the parameters of the log-normal function determined by fitting experimental data to eq 1. The particle dispersion among samples was compared by using the relative standard deviation $RSD = \sigma/D_{TEM}$. The crystal structure of the particles was determined by the analysis of High Resolution TEM images (HR-TEM) and Selected Area Electron Diffraction (SAED) recorded with a JEOL 2100 microscope. The particle interplanar distances were calculated using the Gatan Microscopy Suite® software and compared with X'Pert High Score Plus patterns for bulk Fe_3O_4 (code: 01-086-1337) and bulk FeO (01-077-2355). The interplanar distances (d-space) were calculated measuring the radius between the central spot and the diffracted rings using Image J software[35]. Then the reflections were indexed to (h k l) planes by using as a reference the patterns of bulk Fe_3O_4 (code: 01-086-1337) and bulk FeO (01-077-2355) (see Figure S2 and Table S1 in Supporting Information).

X-ray powder diffraction (XRD). A PANalytical X'Pert PRO MPD diffractometer with Cu Kα radiation ($\lambda = 1.5418$ Å) was used to collect XRD spectra within 10 and 120º of 2θ with a step size of 0.001 or 0.033º of 2θ. The crystal size D_{XRD} was calculated by Rietveld analysis using the FullProf Suite software.[36] $S_{OH}10$, $S7$, $S_{OH}6$ and $S_{OC}6$ samples were fitted to Fe_3O_4 phase (from the Inorganic Crystal Structure Database, ICSD: 158507) and $S_{OC}29$ and $S_{OC}48$ to a mixture of Fe_3O_4/FeO (FeO, ICSD: 82233 phases (see Table 2 and Figure S4 of Supporting Information). Sample $S_{OH}16$ was fitted using the Pattern Matching method for the Fe_3O_4 phase and the Rietveld analysis for the FeO phase.

Inductively Coupled Plasma Optical Emission Spectroscopy (ICP-OES). Aliquots of sample solutions were dried and then digested in 250 µL of HNO_3 (65 %) under 2 h of sonication. Then, the organic residues were separated by filtration, and the remnant was diluted in 25 mL volumetric

flasks with distilled water. Afterwards, the Fe content was determined with a Perkin Elmer

OPTIMA 3200RL. The reaction yield (η) was calculated for each sample as:

$$\eta = \frac{m(Fe)_{sample}}{m(Fe)_o} \times 100 \tag{4}$$

Where $m(Fe)_{sample}$ corresponds to the total mass of iron within the particle composition and was

determined with the following expression:

$$m(Fe)_{sample} = \frac{100\ C_{ICP}}{V_{aliquot}} \tag{5}$$

Here, C_{ICP} and $V_{aliquot}$ correspond to the concentration determined by ICP and the volume for

each aliquot, respectively. Finally, $m(Fe)_o$ stands for the initial mass of Fe utilized in each

reaction.

Superconducting Quantum Interference Device (SQUID) magnetometry. The precipitated

samples were dried with a nitrogen flow, removing the major part of solvents. Secondly, the

resulting powders were kept in vacuum conditions for at least 48 h at room temperature to obtain

compressed pellets. Then, the magnetic measurements were performed encapsulating the pellets

in a gelatin capsule. Magnetic features of the samples in powder were evaluated first by measuring

hysteresis loops $M(H)$ recorded within $\pm$ 5 T at 5 and 300 K. Saturation magnetization (M_S) was

obtained by extrapolation of the high-field region of $M(H)$ to zero field, assuming the high-field

behavior: $M(H) = M_S + \chi_p H$, where χ_p is a residual susceptibility due to paramagnetic species

and/or non collinear spin alignments. M_S values were normalized to the Fe content estimated from

the ICP measurements. The coercive field H_c was obtained as $H_c = (|H_c^+| + |H_c^-|)/2$, where H_c^+

and H_c^- were the intercepts of the hysteresis loop branches with the H-axis.[37] The average

magnetic diameter, D_{mag}, for each series of samples was computed at 300 K from the $M(H)$ curves

because at this temperature the particles are superparamagnetic and interparticle interactions can

be neglected. In this regime, $M(H)$ curves can be fitted to a log-normal distribution $P(m)$ of

Langevin functions $L(x)$ associated with the superparamagnetic behavior of the particles plus a linear-field term caused by the lack of perfect collinearity in the internal ferrimagnetic ordering within the particles and/or at the particle surface, and/or the existence of some residual paramagnetic species.[22]

$$M(H,T) = M_S \frac{\int mP(m)L\left(\frac{mH}{Kk_BT}\right)dm}{\int mP(m)dm} + \chi_p H \qquad (6)$$

Here, m is the magnetization of the crystallites that form the particles, M_s= 468 emu·cm^{-3} (90 emu·g^{-1}) is the saturation magnetization of bulk Fe$_3$O$_4$ at 300 K, k_B is the Boltzmann constant, and χ_p is an effective paramagnetic susceptibility.[22,38] Since $m = M_s V_m$, where V_m is the activation magnetic volume associated with the crystallites, the distribution of V_m for each sample was computed from the fitted $P(m)$.[22,38] Finally, D_{mag} was estimated from the average value of V_m assuming spherical shapes for the activation magnetic volumes (Figure S8 in Supporting Information).

The temperature dependence of the magnetizations $M_{ZFC} - M_{FC}$ was recorded after zero-field cooling/field cooling the samples under a magnetic field of 50 Oe. The presence of different magnetic phases causing intra-particle exchange bias phenomena[39–41] was investigated by studying the shift along the field axis of hysteresis loops recorded at 5 K after field cooling the samples under 10 kOe from room temperature down to 5 K. The exchange bias field was defined as $H_{eb} = (H_c^+ + H_c^-)/2$.

Fourier-transform infrared spectroscopy (FTIR). Aliquots of the reaction mixtures of S7 and S$_{OH}$16 at several reaction stages were studied by a Thermo SCIENTIFIC NICOLET iZ10 infrared spectrometer ranging from 400 to 4000 cm^{-1} with a spectral resolution of 4 cm^{-1}.

Results and discussion

Structural properties of the samples. We have investigated the role played by the amount of both 1-octadecene and 1,2-hexadecanediol on the structural features of iron oxide NPs synthesized by the high-temperature decomposition method of iron (III) acetylacetonate in the presence of oleic acid.[34,42–44]

TEM images for S_{OH} and S_{OC} samples are depicted in Figure 1a-d and Figure 1e-h, respectively. The corresponding particle size distributions are displayed in Figure S1 in Supporting Information. As common trends, both series of samples show particles with narrow size distributions ($RSD \leq$ 0.2) and rounded shapes. In addition, NPs tend to assemble onto the carbon-coated Cu grid avoiding the formation of big aggregates due to the steric forces associated with the oleic acid coating.[45] Moreover, interplanar distances measured on HR-TEM images for all the samples can be attributed to the Fe_3O_4 phase, except for the samples $S_{OC}29$ and $S_{OC}48$, which can be attributed either to Fe_3O_4 or FeO phase (Figure 1 and Figure S2 of Supporting Information) . However, both the size and the crystalline quality of the samples are greatly impacted by the variation of the amount of either 1-octadecene or 1,2-hexadecanediol in the reaction mixture.

Firstly, two types of samples could be distinguished depending on whether they were synthesized with enough amount of 1,2-hexadecanediol in the reaction mixture. For instance, sample $S_{OH}16$ (synthesized without 1,2-hexadecanediol), showed the biggest particles with $D_{TEM} = 15.8 \pm 1.7$ nm. However, $S_{OH}16$ NPs, as displayed in TEM images, contained a lot of crystalline defects (Figure S2 in Supporting Information), due to either the coexistence of two iron oxide phases or the occurrence of different growth planes. In contrast, NPs obtained with an increasing amount of 1,2-hexadecanediol showed single crystal Fe_3O_4 NPs and a progressive reduction in the size down to $D_{TEM} = 6.2 \pm 0.6$ nm for $S_{OH}6$.
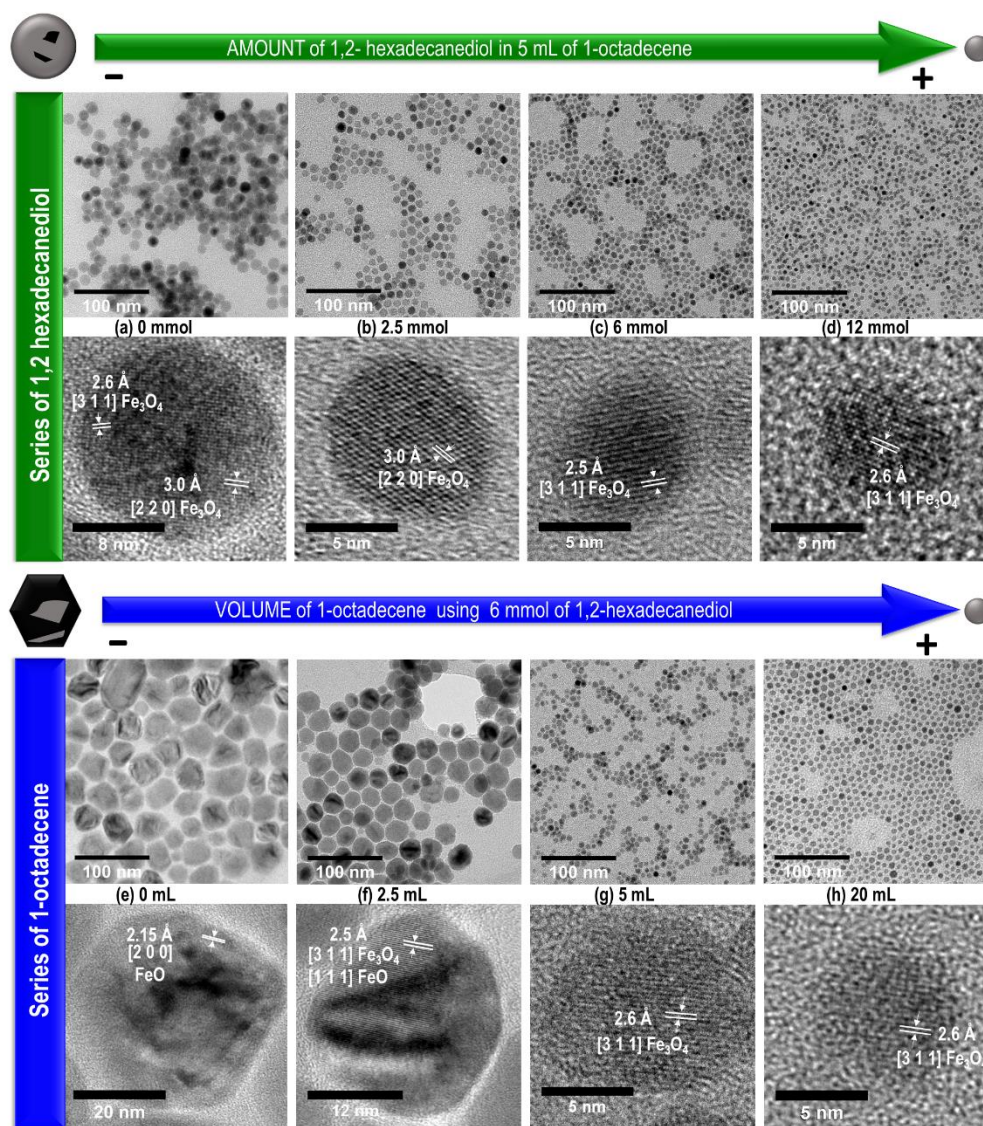
Figure 1. TEM characterization for the series of S_{OH} and S_{OC} samples. Upper panels show TEM images for samples prepared with increasing amounts of 1,2-hexadecanediol in 5 mL of 1-octadecene. (a) $S_{OH}16$ (0mmol), (b) $S_{OH}10$ (2.5 mmol), (c) S7 (6 mmol) and (d) $S_{OH}6$ (12 mmol). Bottom panels display TEM images for increasing volumes of 1-octadecene and 6 mmol of 1,2-hexadecanediol. (e) $S_{OC}48$, (f) $S_{OC}29$, (g) S7 and (h) $S_{OC}6$. Interplanar distances for individual NPs were indexed to atomic planes of the Fe_3O_4 or FeO phase.

Table 1. Experimental conditions to prepare each series of samples together with the TEM characterization and the reaction yield.

Series	Sample	Amount of reagent	Molarity (M)	$D_{TEM} \pm \sigma$ (nm)	RSD	η (%)
S_{OH}	$S_{OH}16$	0 mmol 1,2-hexadecanediol	—	15.8 ± 1.1	0.07	62 ± 2
	$S_{OH}10$	2.5 mmol 1,2-hexadecanediol	0.5	10.1 ± 0.9	0.09	82 ± 3
	S7	6 mmol 1,2-hexadecanediol	1.2	7.4 ± 1.1	0.15	58 ± 1
	$S_{OH}6$	12 mmol 1,2-hexadecanediol	2.4	6.2 ± 0.6	0.10	37 ± 3
S_{OC}	$S_{OC}48$	0 mL 1-octadecene	—	48 ± 9	0.19	65 ± 4
	$S_{OC}29$	2.5 mL 1-octadecene	2.4	25 ± 5 29 ± 2	0.19	58 ± 2
	S7	5 mL 1-octadecene	1.2	7.4 ± 1.1	0.15	58 ± 1
	$S_{OC}6$	20 mL 1-octadecene	0.3	6.7 ± 1.4	0.20	33 ± 1

Secondly, we investigated the effect of the amount of 1-octadecene solvent on the structural features of the samples. A lower amount of the solvent yielded larger NPs exhibiting some edges for $S_{OC}48$ and $S_{OC}29$. These NPs were in fact aggregates of smaller crystallites randomly oriented (see Figure 1e,f). In contrast, NPs obtained with a higher amount of 1-octadecene became single-domain crystals and more spherical in shape (see Figure 1g,h).

As for η, it is observed as a general trend that increasing the amount of both reagents reduces η for both series of S_{OH} and S_{OC} samples. For example, in the series of S_{OC} samples, η decreases from 65% for $S_{OC}48$ to 33 % for $S_{OC}6$ because of the increasing amount of 1-octadecene in the reaction mixture up to 20 mL.
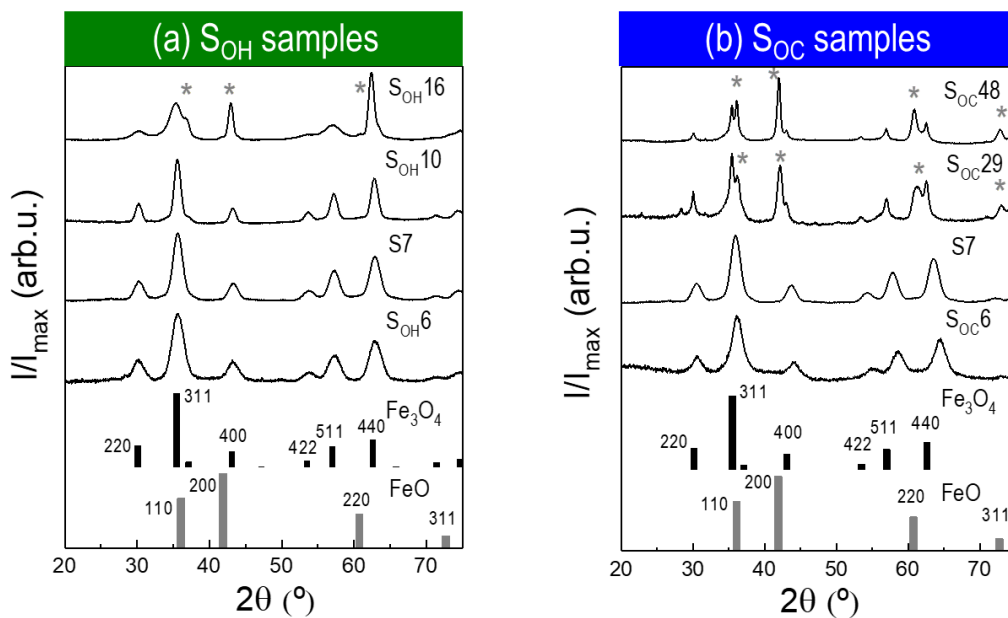
Figure 2. X-ray diffraction spectra. XRD data for the two series of samples: S_{OH} (a) and S_{OC} (b). Vertical black and gray lines at the bottom correspond to X'Pert High Score Plus patterns for bulk Fe_3O_4 and FeO phases with reference codes of 01-086-1337 and 01-077-2355, respectively. Peaks corresponding to atomic planes of the FeO phase are tagged by grey asterisks.

The reaction conditions, together with the main structural parameters for each sample, namely D_{TEM}, σ, and *RSD* from the TEM analysis, and the η are summarized in Table 1.

Next, the SAED measurements showed the possibility of coexistence of two phases of iron oxide, Fe_3O_4 and FeO in the samples $S_{OH}16$, $S_{OC}48$ and $S_{OC}29$ (see Figure S3 and Table S1 in Supporting Information). To obtain more information of the structural features we performed the XRD spectra shown in Figure 2 for S_{OH} and S_{OC} samples. At first glance, XRD diffractograms for both series of samples exhibit two triplets of peaks between 25 and 65º corresponding to the planes (220), (311), (400), (422), (511), and (450), which are associated with γ-Fe_2O_3/Fe_3O_4 phases. Despite this common signature, there are important differences between the XRD spectra for S_{OH} and S_{OC} samples due to the different amounts of either 1,2-hexadecanediol or 1-octadecene used

in their respective reaction mixtures. On the one hand, XRD diffractograms for NPs prepared without or very few of either one of these two reagents show three additional peaks that can be indexed to (111), (200) and (220) planes of FeO (see XRD spectra for samples $S_{OH}16$, $S_{OC}48$ and $S_{OC}29$). On the other hand, two main effects have been found when increasing the amount of either of these two reagents: i) the disappearance of the overreduced FeO phase; and ii) a progressive broadening of the peaks in the XRD pattern indicating a reduction of D_{XRD} (see Table 2).

Table 2. Crystallographic characterization of the samples

Series	Sample	% (Fe_3O_4)	D_{XRD}(Fe_3O_4) $\pm\sigma$ (nm)	% (FeO)	D_{XRD}(FeO) $\pm\sigma$ (nm)
S_{OH}	$S_{OH}16$	Not calculated	5 ± 4	Not calculated	Not calculated
	$S_{OH}10$	100%	9.1 ± 0.2	0%	-
	$S7$	100%	5.97 ± 0.12	0%	-
	$S_{OH}6$	100%	5.75 ± 0.12	0%	-
S_{OC}	$S_{OC}48$	50%	27.5 ± 0.2 7.07 ± 0.17	50%	55.9 ± 1.6
	$S_{OC}29$	65%	21.1 ± 1.4 8.1 ± 1.7	35%	22.6 ± 1.0
	$S7$	100%	5.97 ± 0.12	0%	-
	$S_{OC}6$	100%	7.1 ± 0.3	0%	-

[a] The quantitative percentage of each phase as well as the crystal diameter of the FeO phase could not be calculated because the fitting was done by a combination of the Pattern Matching and Structural Rietveld methods.

To recapitulate this section, either the absence or the use of a small amount of 1,2-hexadecanediol or 1-octadecene leads to the formation of larger NPs with a poor control over their structural features but with a higher η. In contrast, a larger amount of either reagent leads to the formation of single-crystalline NPs, with a progressive reduction of both particle size and η when

the amount of any of these two reagents is above a certain threshold. It is worth noting that the minimum amount of these two reagents to prepare single-crystalline NPs are 2.5 mmol of 1,2-hexadecanediol and 5 mL of 1-octadecene for 1 mmol of $Fe(acac)_3$, which corresponds to sample $S_{OH}10$ (see Table 1).

Elucidating the reaction mechanisms for the series of S_{OH} and S_{OC} samples.

To gain further insight into the reaction mechanisms behind the strong dependence of the structural properties of the samples on the amount of 1,2-hexadecanediol, the reaction mixtures for samples $S_{OH}16$ and S7 were monitored following a methodology described elsewere[27,34] (see Figure S5, S6 and Table S2 in Supporting Information). Briefly, 0.5 mL aliquots were collected for samples $S_{OH}16$ and S7 and analyzed by FTIR spectroscopy at 105 ºC (30 minutes), 200 ºC (0 minutes), 200 ºC (60 minutes), 200 ºC (120 minutes), 310 ºC (0 minutes), 310 ºC (30 minutes), and 310 ºC (60 minutes). As a general trend, characteristics bands of 1-octadecene at 3076 cm^{-1} and 1640 cm^{-1}, corresponding to stretching (=CH-) and (C=C), respectively[46,47] remain constant throughout the reaction process, pointing that most of the 1-octadecene does not react. Moreover, we have found a great impact over the spectral signatures of both the acetylacetonate and oleic acid bands depending on the amount of 1,2-hexadecanediol. At 105 ºC, S7 and $S_{OH}16$ show two bands at 1530 and 1575 cm^{-1} corresponding to the stretching bands of the $Fe(acac)_3$ (C=C and C=O).[48–50] In S7, these two bands vanish at 200 ºC, while for $S_{OH}16$ they remain up to 310ºC. Spectra also show a decrease of the intensity of the band at 1352 cm^{-1} (v_s(COO) of $Fe(acac)_3$) over the reaction course. Next, the band (C=O) of the oleic acid at 1710 cm^{-1} splits and shifts at higher energies in early stages for sample S7, which may be related to the change in the coordination mode of oleic acid and the acetylacetonate after reacting.[48,51–54] This change in the band happens in early stages for the sample S7, but it is delayed for sample $S_{OH}16$. Finally, we focused on the

evolution of bands corresponding to 1,2-hexadecanediol to elucidate the role of this reagent on the reaction mechanism. First, the band at 3347 cm^{-1} (stretching O-H) disappears at 200 °C.[55,56] Second, bands assigned to C-O stretching,[55,56] ranging from 1217 to 1067 cm^{-1}, become broader and less intense likely because of the diminution of the concentration of this reagent in the reaction content. To summarize the effect of 1,2-hexadecanediol, the formation of NPs is affected by the presence of this reagent in two ways. First, it accelerates the decomposition of Fe(acac)$_3$ at earlier reaction stages leading to an enhancement of the number of iron oxide nuclei. Second, the amount of the iron complex after the nucleation decreases, and consequently, the growth stage of the NPs is driven by a low diffusion mechanism yielding smaller NPs with high crystal quality. In contrast, the absence of 1,2-hexadecanediol in the reaction mixture leads to a reduction in the number of available nuclei and to a higher concentration of the iron complex. Under these conditions, the reaction mechanism proceeds by the coalescence of various nuclei following a faster aggregation process and generating larger NPs but with poorer control over their crystalline structure (Figure 1a, Table 2 and Figure S2 in the Supporting Information).[9,57]

Since variations on the precursor concentration tends to alter the balance of the activation energy, we have monitored the structural properties of S$_{OH}$ and S$_{OC}$ samples as a function of their concentrations. These results are summarized in Table 1 and 2. [58,59] At first glance, it is found that [1,2-hexadecanediol] ≥ 0.5 M and [oleic acid] ≤ 1.2 M lead to spherical, monophasic, single crystalline NPs. Here, the thermodynamic contribution becomes more important and thus particle growth slows down. In addition, a spherical shape is favored to minimize the NP surface energy.[58] On the contrary, the formation of edges on samples S$_{OC}$48 and S$_{OC}$29 (Figure 1e,f) is caused by a faster growth, where the kinetic contribution is dominant. Here, a larger amount of oleic acid favors a selective and stronger bonding at the low-energy facets (100).[60] As a consequence, the growth is

hampered along the [100] direction and favored along the [111] direction.[28,60–62] Besides, the low solvent volume has a dramatic effect on the size distribution. Testa-Anta et al.[60] recently suggested that the high amount of CO_2 generated due to the high concentration of oleic acid limits both the decomposition of the iron precursor and the subsequent nucleation while favors the growth of the NPs.[60] Samples $S_{OC}29$ and $S_{OC}16$ (Figure S1 in Supporting Information) with only 2.5 mL and 1 mL, respectively, show bimodal distributions probably because of an incomplete Ostwald ripening.[58,63–65] The high concentration of particles may hamper the diffusion of materials through the solution and thus the small particles remain longer in the solution leading to bimodal size populations.

Furthermore, the presence of FeO in samples $S_{OH}16$, $S_{OC}29$, and $S_{OC}48$ (see XRD spectra in Figure 2 and Figure S4 of Supporting Information) may be due to an excess of carbon monoxide (CO) in the reaction mixture as it is explained by Hai et al.[31] CO is a strong reductant gas that can lead to an overreduction from iron (III) to iron (II).[31] Figure 3 summarizes the insights into the morphology and the oxidation state of iron oxide NPs by monitoring the amount of either 1,2-hexadecanediol or 1-octadecene in the reaction mixture. A low amount of either compound yields to larger $Fe_{3-x}O_4$ NPs containing FeO as a secondary phase, because of a faster particle growth driven by kinetics[58,59] and associated with the overreduction from iron (III) to iron (II). It is worth noting that the FeO fraction can be comparable to that of the $Fe_{3-x}O_4$, being the average crystallite size even larger than the $Fe_{3-x}O_4$ one in very inhomogeneous samples, such as $S_{OC}48$. In contrast, a larger amount of either 1,2-hexadecanediol or 1-octadecene leads to small, spherical and single phase NPs due to a slow particle growth driven by thermodynamics.[58,59]
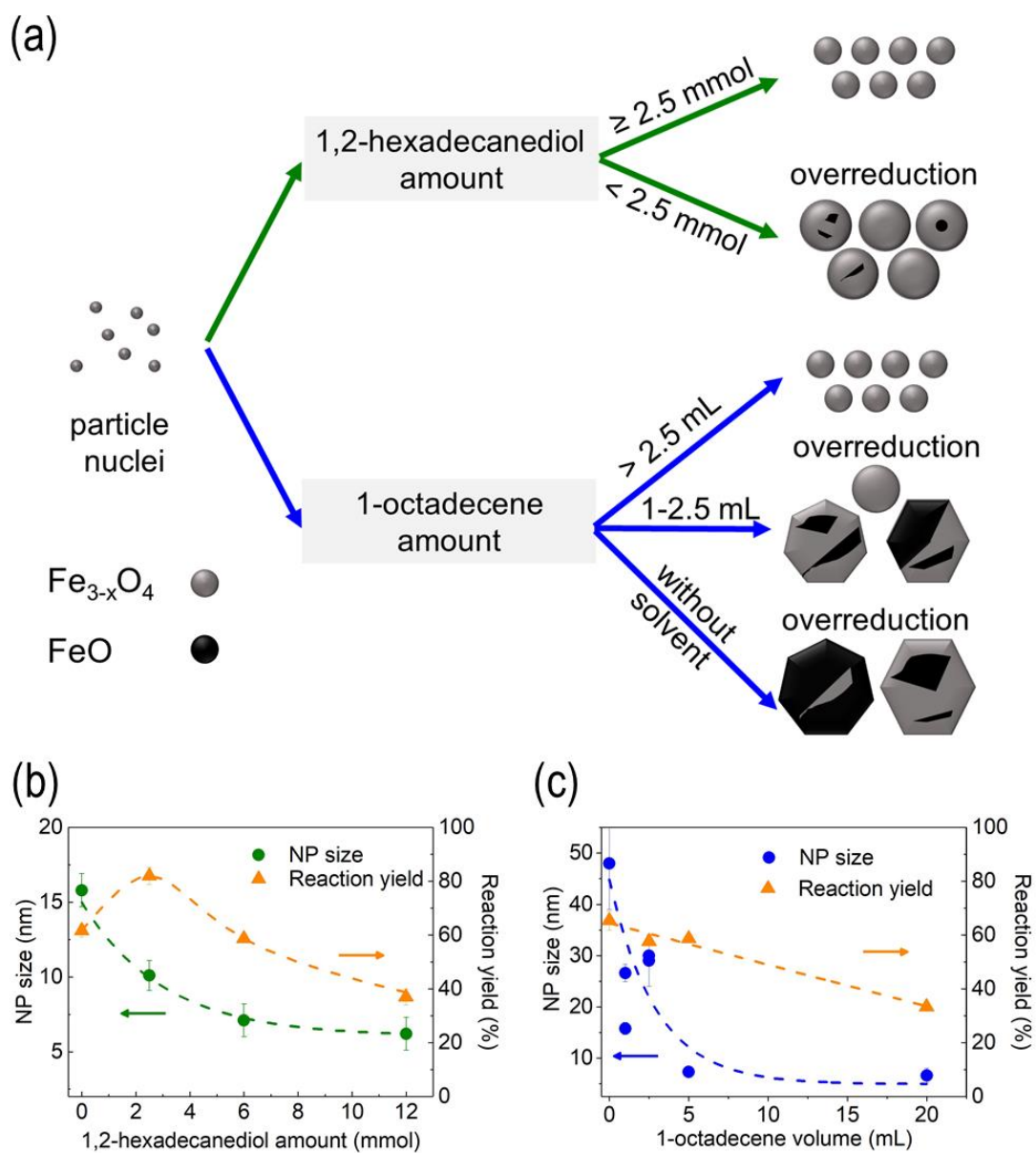
Figure 3. The effect of the amount of either 1,2-hexadecanediol or 1-octadecene on the morphology, oxidation state, and reaction yield of iron oxide NPs prepared by the thermal decomposition of Fe(acac)₃ in oleic acid. (a) Schematic representation of the formation of iron oxide NPs as a function of the amount of 1,2-hexadecanediol (green) or 1-octadecene (blue). (b), (c) Dependence of the particle size and reaction yield with the amount of 1,2-hexadecanediol and 1-octadecene, respectively.

The impact of the morphology, crystal quality, and oxidation states on the magnetic properties of the series of S$_{OH}$ and S$_{OC}$ samples. The effect of the crystalline microstructure on the properties of S$_{OH}$ and S$_{OC}$ samples was also evaluated by studying the magnetism of the NPs. The results obtained from the magnetic characterization which are included in Table 3 are as follows: H_c and M_s from $M(H)$ curves at 5 and 300 K, H_{eb} at 5K, D_{mag} computed by fitting $M(H)$ curves at 300 K to eq 6, and the peak temperature T_p in the M_{ZFC} curves.

$M(H)$ curves at 5 and 300 K for S$_{OH}$ and S$_{OC}$ samples show different magnetic behavior (Figure S7 of Supporting Information). On the one hand, NPs with $D_{TEM} \leq 10$ nm exhibit a slightly lower M_s than the Fe$_3$O$_4$ bulk value, which indicates a bulk-like, ferrimagnetic (FiM) spin alignment throughout the whole NP.[24,25,38,43] Besides, H_c increases with the particle volume up to the expected values for single domain NPs in this range of sizes[23,25]. On the other hand, bigger NPs show a large enhancement of H_c together with a very significant reduction of M_s due to the coexistence of FeO (AFM) and Fe$_3$O$_4$ (FiM) phases within the particle structure.[32,40,41,66] A further insight into the FiM order was gained by the determination of D_{mag} obtained from the fits of the $M(H)$ curves at 300 K to a distribution of Langevin functions (see eq 7 and Figure S8 in the Supporting Information).[22] Details on these fits are provided in the experimental section. At 300 K, most of the samples are in the superparamagnetic state; except S$_{OC}$48 and S$_{OC}$29, since they contain a significant amount of thermally blocked NPs because their size distributions are centered at much greater volumes. Here, we can distinguish two types of samples depending on the particle size and composition. While D_{mag} for samples with $D_{TEM} \leq 10$ nm are similar to D_{XRD} because they are composed entirely of single-phase, single crystalline Fe$_3$O$_4$ NPs, S$_{OH}$16 exhibits a $D_{mag} \approx D_{TEM}/4$ due to the inclusion of FeO crystallites within the NPs.[40,42–44,66]

Table 3. Magnetic properties for samples S_{OH} and S_{OC} measured in powder.

Series	Sample	H_c at 5 K (kOe)	M_s at 5 K (emu/g Fe)	H_c at 300 K (kOe)	M_s at 300 K (emu/g Fe)	$D_{mag} \pm \sigma$ (nm)	T_P (K)
S_{OH}	$S_{OH}16$	0.80 ± 0.01	66 ± 2	SPM	62 ± 2	4.2 ± 2.4	190
	$S_{OH}10$	0.40 ± 0.01	115 ± 4	SPM	102 ± 3	7.0 ± 0.7	131
	S7	0.23 ± 0.02	110 ± 3	SPM	90 ± 3	5.9 ± 0.9	45
	$S_{OH}6$	0.087 ± 0.01	100 ± 3	SPM	77 ± 2	4.7 ± 0.7	20
S_{OC}	$S_{OC}48$	0.78 ± 0.02	69 ± 2	0.168 ± 0.002	66 ± 2	---	---
	$S_{OC}29$	0.61 ± 0.01	63 ± 2	0.038 ± 0.002	61 ± 2	---	---
	S7	0.23 ± 0.02	110 ± 3	SPM	90 ± 3	5.9 ± 0.9	45
	$S_{OC}6$	0.18 ± 0.01	100 ± 3	SPM	83 ± 3	5.8 ± 0.6	45

Figure 4 shows M_{ZFC}/M_{FC} curves measured under $H = 50$ Oe. Some general trends can be identified as a function of the particle size. Small NPs with $D_{TEM} \leq 16$ nm show typical features of superparamagnetism.[22,38] In particular, M_{ZFC} curves exhibit a single peak located at $T_p < 200$ K that shifts towards higher temperatures with the particle volume because the Néel relaxation is the dominant activation mechanism for single domain NPs within this size range.[22,38] In contrast, samples $S_{OC}29$ and $S_{OC}48$ exhibit broader M_{ZFC}/M_{FC} curves with some plateaus and shoulders but without any clear sign of the characteristic peak related to the particle blocking, since T_p must be above room temperature for such large particles. Figure S9 in Supporting Information displays the first derivative of M_{ZFC} curves for $S_{OC}29$ and $S_{OC}48$ samples. Both derivatives show two sharp peaks associated with the signatures of the Fe_3O_4 and FeO phases within the NPs. Firstly, there is

a sharp peak at 86 and 105 K for $S_{OC}29$ and $S_{OC}48$, respectively, likely associated with the Verwey transition (T_V) in Fe_3O_4.[32,40,42–44,66,67] Note that T_V is only present in NPs with $D \geq 10$ nm and with a stoichiometry very close to that of perfect Fe_3O_4. Furthermore, both derivatives show a second peak at 237 and 221 K for $S_{OC}29$ and $S_{OC}48$, respectively, likely related to the Néel transition (T_N) associated with the AFM phase in FeO.[32,40,42–44,66] Finally, hysteresis loops were recorded at 5 K after field cooling $S_{OH}16$ and $S_{OC}48$ samples from room temperature under 10 kOe (see Figure 5). Both $S_{OH}16$ and $S_{OC}48$ samples show shifted loops along the H-axis with $H_{eb} \approx 1$ and 1.07 kOe, respectively, likely due to the exchange coupling between the FiM and AFM phases coexisting within the NPs.[32,40,42–44,66]
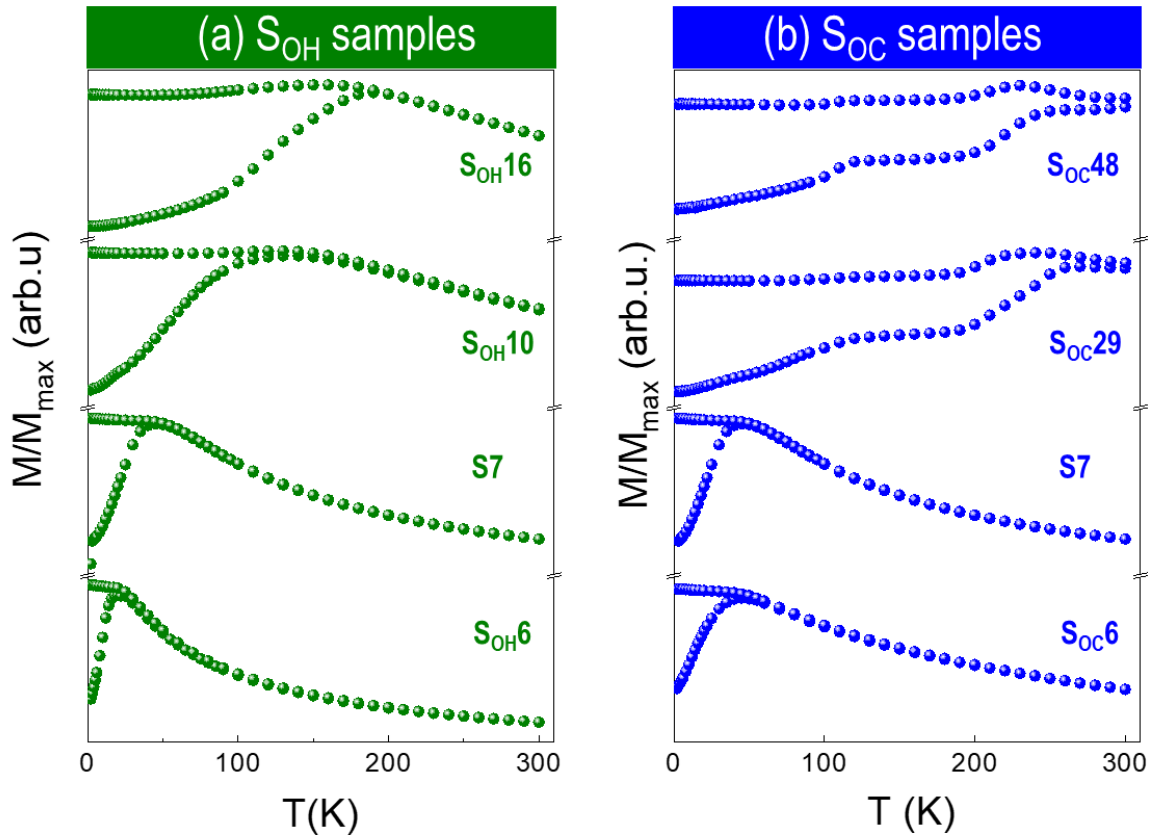
Figure 4. M_{ZFC}/M_{FC} curves at $H = 50$ Oe for the series of S_{OH} and S_{OC} samples. Samples from top to bottom for (a) S_{OH}: $S_{OH}16$, $S_{OH}10$, S7 and $S_{OH}6$. (b) S_{OC}: $S_{OC}48$, $S_{OC}29$, S7 and $S_{OC}6$. The

corresponding curves for S_OH and S_OH samples are depicted with green and blue solid spheres, respectively.

To summarize this section, magnetic features for samples S_OH and S_OC correlate well to their structural properties. Briefly, NPs with $D_{TEM} \leq 10\,\text{nm}$ show typical features of superparamagnetism: $H_c = 0$ at 300 K, and T_p are well below room temperature. Besides, these samples exhibit a M_s slightly lower than that of bulk Fe_3O_4 and $H_{eb} = 0$. These results suggest that samples with $D_{TEM} \leq 10\,\text{nm}$ are made up of monophasic, single-crystalline $Fe_{3-x}O_4$ NPs. In contrast, larger NPs show a reduced M_s by around 40%, the signature of a Néel transition in the M_{ZFC}/M_{FC} curves, and $H_{eb} \approx 1\,\text{kOe}$, all these features likely caused by the presence of FeO crystallites within the NPs.
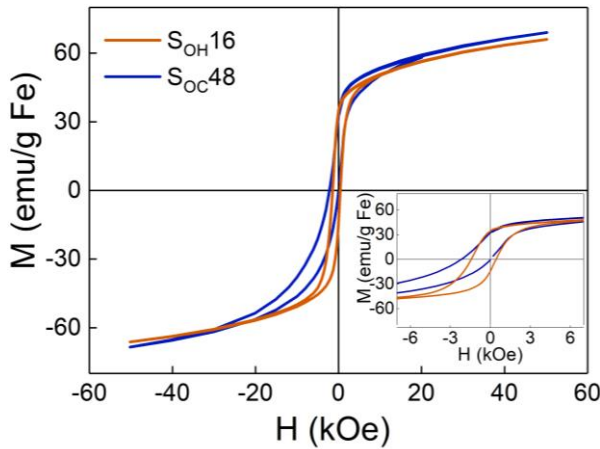
Figure 5. Magnetization as a function of the magnetic field recorded after field cooling samples S_OH16 and S_OC48 under 10 kOe from 300 K down to 5 K. Samples S_OH16 and S_OC48 are depicted as orange and blue lines, respectively. Inset shows the low field region within $H = \pm 7$ kOe.

Conclusions

We have shown the effect of the amount of 1,2-hexadecanediol and 1-octadecene on the synthesis of iron oxide NPs with sizes ranging from 6 to 48 nm by the high temperature decomposition of Fe(acac)$_3$ using oleic acid as surfactant. We have demonstrated an accurate control over the particle structure by a rational monitoring of the amount of 1,2-hexadecanediol and 1-octadecene in the reaction mixture. On the one hand, we have shown that a low amount of either of the two reagents results in large NPs containing both Fe$_3$O$_4$ and FeO phases but with high values of the reaction yield. On the other hand, a higher amount of one of the reagents gives rise to NPs with $D \leq 10$ nm, composed of single-phase, single-crystalline Fe$_3$O$_4$, but with moderate yield values. Moreover, we have found that, for 1 mmol of iron (III) acetylacetonate, the minimum amount of 1,2-hexadecanediol and 1-octadecene for the preparation of monophasic, single-crystalline Fe$_3$O$_4$ NPs are 2.5 mmol and 5 mL, respectively. By monitoring the reaction conditions, we have shown that the presence of 1,2-hexadecanediol accelerates the decomposition of Fe(acac)$_3$ at earlier reaction stages; thus, decreasing the amount of the iron complex after the nucleation. Consequently, the growth of the NPs is driven by a low diffusion mechanism yielding smaller NPs of high crystalline quality. Although 1-octadecene does not actively participate in the reaction mechanism, variations on the concentrations of this solvent yield dramatic changes on the final particle structure.

Structural and magnetic properties have also been correlated for both series of samples. First, we have found that small NPs show typical features of superparamagnetism: M_s values are very close to that of bulk Fe$_3$O$_4$ and D_{mag} is very similar to D_{TEM}. In addition, $H_c = 0$ at 300 K and $T_p < 300$ K in M_{ZFC} curves. Second, larger NPs composed of Fe$_3$O$_4$ and FeO phases exhibit a very significant reduction of M_s, and H_{eb} values around 1 kOe. In addition, M_{ZFC}/M_{FC} curves show two anomalies associated with T_v and T_N because of the biphasic nature of the NPs.

Overall, we show that an optimal reagent control in the thermal decomposition process enables the synthesis of iron oxide nanoparticles of selective morphology, crystal microstructure, oxidation state and magnetic response, with narrow size distributions and good reaction yields.

Our work adds an extra level of optimization, both from a fundamental and an applied perspective, in the quest for outstanding candidates for multifunctional nanoparticle agents for their use in magnetic recoverable catalysts or biomedical applications.

ASSOCIATED CONTENT

Supporting Information. The following files are available free of charge.

The particle size distributions fittings, HR-TEM image analysis, SAED analysis, whole XRD pattern analysis, FTIR spectra, magnetization as function of the magnetic field, Langevin fittings, first derivative of M_{ZFC} curves (PDF)

AUTHOR INFORMATION

Corresponding Author

*cmoyaalv@ulb.ac.be

Author Contributions

The manuscript was written through contributions of all authors. All authors have given approval to the final version of the manuscript.

ACKNOWLEDGMENT

ABBREVIATIONS

η, reaction yield; acac, acetylacetonate; AFM, antiferromagnetic; FiM, ferrimagnetic; FTIR, Fourier-transform infrared spectroscopy; HR-TEM: High Resolution Transmission Electron Microscopy; ICP-OES, Inductively Coupled Plasma Optical Emission Spectroscopy; NPs, nanoparticles; RSD. Relative Standard Deviation; SAED, Selected Area Electron Diffraction; SQUID, Superconducting Quantum Interference Device; TEM, Transmission Electron Microscopy; XRD, X-ray powder diffraction

REFERENCES

(1)   Tudosa, I.; Stamm, C.; Kashuba, A. B.; King, F.; Siegmann, H. C.; Stöhr, J.; Ju, G.; Lu, B.; Weeler, D. The Ultimate Speed of Magnetic Switching in Granular Recording Media. *Nature* **2004**, *428* (6985), 831–833.

(2)   Liu, Y.; Jiang, Y.; Zhang, X.; Wang, Y.; Zhang, Y.; Liu, H.; Zhai, H.; Liu, Y.; Yang, J.; Yan, Y. Effects of Annealing Temperature on the Structure and Magnetic Properties of the $L1_0$-FePt Nanoparticles Synthesized by the Modified Sol-Gel Method. *Powder Technol.* **2013**, *239*, 217–222.

(3)   Bansmann, J.; Baker, S. H.; Binns, C.; Blackman, J. A.; Bucher, J. P.; Dorantes-Dávila, J.; Dupuis, V.; Favre, L.; Kechrakos, D.; Kleibert, A.; Meiwes-Broer, K. H.; Pastor, G. M.; Perez, A.; Toulemonde, O.; Trohidou, K. N.; Tuaillon, J.; Xie, Y. Magnetic and Structural

Properties of Isolated and Assembled Clusters. *Surf. Sci. Rep.* **2005**, *56* (6–7), 189–275.

(4)   Gallo-Cordova, A.; Lemus, J.; Palomares, F. J.; Morales, M. P.; Mazarío, E. Superparamagnetic Nanosorbent for Water Purification: Assessment of the Adsorptive Removal of Lead and Methyl Orange from Aqueous Solutions. *Sci. Total Environ.* **2020**, *711*, 134644.

(5)   Perez, J. M.; Josephson, L.; Weissleder, R. Use of Magnetic Nanoparticles as Nanosensors to Probe for Molecular Interactions. *ChemBioChem* **2004**, *5* (3), 261–264.

(6)   Sun, C.; Lee, J. S. H.; Zhang, M. Magnetic Nanoparticles in MR Imaging and Drug Delivery. *Adv. Drug Deliv. Rev.* **2008**, *60* (11), 1252–1265.

(7)   Mejías, R.; Pérez-Yagüe, S.; Roca, A. G.; Pérez, N.; Villanueva, Á.; Cañete, M.; Mañes, S.; Ruiz-Cabello, J.; Benito, M.; Labarta, A.; Batlle, X.; Veintemillas-Verdaguer, S.; Morales, M. P.; Barber, D. F.; Serna, C. J. Liver and Brain Imaging through Dimercaptosuccinic Acid-Coated Iron Oxide Nanoparticles. *Nanomedicine* **2010**, *5* (3), 397–408.

(8)   Pankhurst, Q. A.; Connolly, J.; Jones, S. K.; Dobson, J. Applications of Magnetic Nanoparticles in Biomedicine. *J. Phys. D. Appl. Phys.* **2003**, *36*, R167–R181.

(9)   Roca, A. G.; Costo, R.; Rebolledo, A. F.; Veintemillas-Verdaguer, S.; Tartaj, P.; González-Carreño, T.; Morales, M. P.; Serna, C. J. Progress in the Preparation of Magnetic Nanoparticles for Applications in Biomedicine. *J. Phys. D. Appl. Phys.* **2009**, *42* (22), 224002.

(10)   Shifrina, Z. B.; Bronstein, L. M. Magnetically Recoverable Catalysts: Beyond Magnetic Separation. *Front. Chem.* **2018**, *6*, 298.

(11) Perez, J. M.; O'Loughin, T.; Simeone, F. J.; Weissleder, R.; Josephson, L. DNA-Based Magnetic Nanoparticle Assembly Acts as a Magnetic Relaxation Nanoswitch Allowing Screening of DNA-Cleaving Agents. *J. Am. Chem. Soc.* **2002**, *124* (12), 2856–2857.

(12) Koh, I.; Hong, R.; Weissleder, R.; Josephson, L. Sensitive NMR Sensors Detect Antibodies to Influenza. *Angew. Chemie Int. Ed.* **2008**, *47* (22), 4119–4121.

(13) Lee, H.; Yoon, T. J.; Weissleder, R. Ultrasensitive Detection of Bacteria Using Core-Shell Nanoparticles and an NMR-Filter System. *Angew. Chemie - Int. Ed.* **2009**, *48* (31), 5657–5660.

(14) Zhang, R.; Wang, X.; Wu, C.; Song, M.; Li, J.; L, G.; Zhou, J.; Chen, C.; Dai, Y.; Gao, F. Synergistic Enhancement Effect of Magnetic Nanoparticles on Anticancer Drug Accumulation in Cancer Cells. *Nanotechnology* **2006**, *17*, 3622.

(15) McCarthy, J. R.; Jaffer, F. A.; Weissleder, R. A Macrophage-Targeted Theranostic Nanoparticle for Biomedical Applications. *Small* **2006**, *2* (8–9), 983–987.

(16) Colombo, M.; Carregal-Romero, S.; Casula, M. F.; Gutiérrez, L.; Morales, M. P.; Böhm, I. B.; Heverhagen, J. T.; Prosperi, D.; Parak, W. J. Biological Applications of Magnetic Nanoparticles. *Chem. Soc. Rev.* **2012**, *41* (11), 4306–4334.

(17) Foy, S. P.; Manthe, R. L.; Foy, S. T.; Dimitrijevic, S.; Krishnamurthy, N.; Labhasetwar, V. Optical Imaging and Magnetic Field Targeting of Magnetic Nanoparticles in Tumors. *ACS Nano* **2010**, *4* (9), 5217–5224.

(18) Ali, Z.; Abbasi, A. Z.; Zhang, F.; Arosio, P.; Lascialfari, A.; Casula, M. F.; Wenk, A.; Kreyling, W.; Plapper, R.; Seidel, M.; Niessner, R.; Knöll, J.; Seubert, A.; Parak, W. J.

Multifunctional Nanoparticles for Dual Imaging. *Anal. Chem.* **2011**, *83* (8), 2877–2882.

(19)   Lee, H. Y.; Li, Z.; Chen, K.; Hsu, A. R.; Xu, C.; Xie, J.; Sun, S.; Chen, X. PET/MRI Dual-Modality Tumor Imaging Using Arginine-Glycine-Aspartic (RGD)-Conjugated Radiolabeled Iron Oxide Nanoparticles. *J. Nucl. Med.* **2008**, *49* (8), 1371–1379.

(20)   Kim, B. H.; Lee, N.; Kim, H.; An, K.; Park, Y. Il; Choi, Y.; Shin, K.; Lee, Y.; Kwon, S. G.; Na, H. Bin; Park, J. G.; Ahn, T. Y.; Kim, Y. W.; Moon, W. K.; Choi, S. H.; Hyeon, T. Large-Scale Synthesis of Uniform and Extremely Small-Sized Iron Oxide Nanoparticles for High-Resolution T_1 Magnetic Resonance Imaging Contrast Agents. *J. Am. Chem. Soc.* **2011**, *133* (32), 12624–12631.

(21)   Batlle, X.; Labarta, A. Finite-Size Effects in Fine Particles: Magnetic and Transport Properties. *J. Phys. D. Appl. Phys.* **2002**, *35*, 15–42.

(22)   Bean, C. P.; Livingston, J. D. Superparamagnetism. *J. Appl. Phys.* **1959**, *30* (4), S120–S129.

(23)   Batlle, X.; Pérez, N.; Guardia, P.; Iglesias, O.; Labarta, A.; Bartolomé, F.; Garca, L. M.; Bartolomé, J.; Roca, A. G.; Morales, M. P.; Serna, C. J. Magnetic Nanoparticles with Bulklike Properties (Invited). *J. Appl. Phys.* **2011**, *109* (7), 1–7.

(24)   Pérez, N.; Bartolomé, F.; García, L. M.; Bartolomé, J.; Morales, M. P.; Serna, C. J.; Labarta, A.; Batlle, X. Nanostructural Origin of the Spin and Orbital Contribution to the Magnetic Moment in $Fe_{3-x}O_4$ Magnetite Nanoparticles. *Appl. Phys. Lett.* **2009**, *94* (9), 4–7.

(25)   Guardia, P.; Batlle-Brugal, B.; Roca, A. G.; Iglesias, O.; Morales, M. P.; Serna, C. J.; Labarta, A.; Batlle, X. Surfactant Effects in Magnetite Nanoparticles of Controlled Size. *J. Magn. Magn. Mater.* **2007**, *316* (2), e756–e759.

(26) Guardia, P.; Pérez, N.; Labarta, A.; Batlle, X. Controlled Synthesis of Iron Oxide Nanoparticles over a Wide Size Range. *Langmuir* **2010**, *26* (8), 5843–5847.

(27) Moya, C.; Batlle, X.; Labarta, A. The Effect of Oleic Acid on the Synthesis of $Fe_{3-x}O_4$ Nanoparticles over a Wide Size Range. *Phys. Chem. Chem. Phys.* **2015**, *17* (41), 27373–27379.

(28) Yang, J.; Kou, Q.; Liu, Y.; Wang, D.; Lu, Z.; Chen, L.; Zhang, Y.; Wang, Y.; Zhang, Y.; Han, D.; Xing, S. G. Effects of Amount of Benzyl Ether and Reaction Time on the Shape and Magnetic Properties of Fe_3O_4 Nanocrystals. *Powder Technol.* **2017**, *319*, 53–59.

(29) Rodríguez, A. F.; Moya, C.; Escoda-Torroella, M.; Romero, A.; Labarta, A.; Batlle, X. Probing the Variability in Oxidation States of Magnetite Nanoparticles by Single-Particle Spectroscopy. *J. Mater. Chem. C* **2018**, *6* (4), 875–882.

(30) Kemp, S. J.; Ferguson, R. M.; Khandhar, A. P.; Krishnan, K. M. Monodisperse Magnetite Nanoparticles with Nearly Ideal Saturation Magnetization. *RSC Adv.* **2016**, *6* (81), 77452–77464.

(31) Hai, H. T.; Yang, H. T.; Kura, H.; Hasegawa, D.; Ogata, Y.; Takahashi, M.; Ogawa, T. 2. pd. Size Control and Characterization of Wustite (Core)/Spinel (Shell) Nanocubes Obtained by Decomposition of Iron Oleate Complex. *J. Colloid Interface Sci.* **2010**, *346* (1), 37–42.

(32) Khurshid, H.; Li, W.; Chandra, S.; Phan, M. H.; Hadjipanayis, G. C.; Mukherjee, P.; Srikanth, H. Mechanism and Controlled Growth of Shape and Size Variant Core/Shell FeO/Fe_3O_4 Nanoparticles. *Nanoscale* **2013**, *5* (17), 7942–7952.

(33) Redl, F. X.; Black, C. T.; Papaefthymiou, G. C.; Sandstrom, R. L.; Yin, M.; Zeng, H.;

Murray, C. B.; O'Brien, S. P. Magnetic, Electronic, and Structural Characterization of Nonstoichiometric Iron Oxides at the Nanoscale. *J. Am. Chem. Soc.* **2004**, *126* (44), 14583–14599.

(34) Moya, C.; Morales, M. D. P.; Batlle, X.; Labarta, A. Tuning the Magnetic Properties of Co-Ferrite Nanoparticles through the 1,2-Hexadecanediol Concentration in the Reaction Mixture. *Phys. Chem. Chem. Phys.* **2015**, *17* (19), 13143–13149.

(35) Schneider, C. A.; Rasband, W. S.; Eliceiri, K. W. NIH Image to ImageJ: 25 Years of Image Analysis. *Nat. Methods* **2012**, *9* (7), 671–675.

(36) Rodriguez-Carvajal, J.; Roisnel, T. FullProf.98 and WinPLOTR New Windows 99/NT Applications for Diffraction. *Int. Union Crystallogr. Newletter* **1998**, *20*, 35–36.

(37) Batlle, X.; García Del Muro, M.; Tejada, J.; Pfeiffer, H.; Görnert, P.; Sinn, E. Magnetic Study of M-Type Doped Barium Ferrite Nanocrystalline Powders. *J. Appl. Phys.* **1993**, *74* (5), 3333–3340.

(38) Cullity, B. D.; Graham, C. D. *Introduction to Magnetic Materials*; John Wiley & Sons, Inc.: Hoboken, NJ, USA, 2008.

(39) Phan, M. H.; Alonso, J.; Khurshid, H.; Lampen-Kelley, P.; Chandra, S.; Repa, K. S.; Nemati, Z.; Das, R.; Iglesias, Ó.; Srikanth, H. Exchange Bias Effects in Iron Oxide-Based Nanoparticle Systems. *Nanomaterials* **2016**, *6* (11), 221.

(40) Nogués, J.; Sort, J.; Langlais, V.; Skumryev, V.; Suriñach, S.; Muñoz, J. S.; Baró, M. D. Exchange Bias in Nanostructures. *Phys. Rep.* **2005**, *422* (3), 65–117.

(41) Iglesias, Ò.; Labarta, A.; Batlle, X. Exchange Bias Phenomenology and Models of

Core/Shell Nanoparticles. *J. Nanosci. Nanotechnol.* **2008**, *8* (6), 2761–2780.

(42)   Sharma, S. K.; Vargas, J. M.; Pirota, K. R.; Kumar, S.; Lee, C. G.; Knobel, M. Synthesis and Ageing Effect in FeO Nanoparticles: Transformation to Core – Shell FeO/Fe_3O_4 and Their Magnetic Characterization. *J. Alloys Compd.* **2011**, *509* (22), 6414–6417.

(43)   Estrader, M.; López-Ortega, A.; Golosovsky, I. V.; Estradé, S.; Roca, A. G.; Salazar-Alvarez, G.; López-Conesa, L.; Tobia, D.; Winkler, E.; Ardisson, J. D.; Macedo, W. A. A.; Morphis, A.; Vasilakaki, M.; Trohidou, K. N.; Gukasov, A.; Mirebeau, I.; Makarova, O. L.; Zysler, R. D.; Peiró, F.; Baró, M. D.; Bergström, L.; Nogués, J. Origin of the Large Dispersion of Magnetic Properties in Nanostructured Oxides: Fe_xO/Fe_3O_4 Nanoparticles as a Case Study. *Nanoscale* **2015**, *7* (7), 3002–3015.

(44)   Kolhatkar, A. G.; Jamison, A. C.; Litvinov, D.; Willson, R. C.; Lee, T. R. Tuning the Magnetic Properties of Nanoparticles. *Int. J. Mol. Sci.* **2013**, *14* (8), 15977–16009.

(45)   Moya, C.; Abdelgawad, A. M.; Nambiar, N.; Majetich, S. A. Magnetic Properties of Cube-Shaped Fe_3O_4 Nanoparticles in Dilute, 2D, and 3D Assemblies. *J. Phys. D. Appl. Phys.* **2017**, *50* (32), 325003.

(46)   Spectral Database For Organic Compounds (SDBS). 1-Octadecene https://sdbs.db.aist.go.jp/sdbs/cgi-bin/landingpage?sdbsno=2669.

(47)   Chapter 4 - Alkenes and Other Compounds Containing C=C Double Bonds. In *Interpreting Infrared, Raman, and Nuclear Magnetic Resonance Spectra*; Nyquist, R. A., Ed.; Academic Press: San Diego, 2001; pp 55–91.

(48)   Spectral Database For Organic Compounds (SDBS). Iron(III) acetylacetonate

https://sdbs.db.aist.go.jp/sdbs/cgi-bin/landingpage?sdbsno=4155.

(49)   Diaz-Acosta, I.; Baker, J.; Cordes, W.; Pulay, P. Calculated and Experimental Geometries and Infrared Spectra of Metal Tris-Acetylacetonates: Vibrational Spectroscopy as a Probe of Molecular Structure for Ionic Complexes. Part I. *J. Phys. Chem. A* **2001**, *105* (1), 238–244.

(50)   Lawson, K. E. The Infrared Absorption Spectra of Metal Acetylacetonates. *Spectrochim. Acta* **1961**, *17* (3), 248–258.

(51)   Spectral Database For Organic Compounds (SDBS). Oleic acid https://sdbs.db.aist.go.jp/sdbs/cgi-bin/landingpage?sdbsno=1035.

(52)   Chapter 14 - Ketones. In *Interpreting Infrared, Raman, and Nuclear Magnetic Resonance Spectra*; Nyquist, R. A., Ed.; Academic Press: San Diego, 2001; pp 287–330.

(53)   Chapter 10 - Carboxylic Acids. In *Interpreting Infrared, Raman, and Nuclear Magnetic Resonance Spectra*; Nyquist, R. A., Ed.; Academic Press: San Diego, 2001; pp 165–203.

(54)   Chapter 15 - Carboxylic Acid Esters. In *Interpreting Infrared, Raman, and Nuclear Magnetic Resonance Spectra*; Nyquist, R. A., Ed.; Academic Press: San Diego, 2001; pp 331–390.

(55)   Chapter 7 - Alcohols and Phenols. In *Interpreting Infrared, Raman, and Nuclear Magnetic Resonance Spectra*; Nyquist, R. A., Ed.; Academic Press: San Diego, 2001; pp 125–141.

(56)   Spectral Database For Organic Compounds (SDBS). 1,2-hexadecanediol ttps://sdbs.db.aist.go.jp/sdbs/cgi-bin/landingpage?sdbsno=1035.

(57) Lamer, V. K.; Dinegar, R. H. Theory, Production and Mechanism of Formation of Monodispersed Hydrosols. *J. Am. Chem. Soc.* **1950**, *72* (11), 4847–4854.

(58) Park, J.; Joo, J.; Soon, G. K.; Jang, Y.; Hyeon, T. Synthesis of Monodisperse Spherical Nanocrystals. *Angew. Chemie - Int. Ed.* **2007**, *46* (25), 4630–4660.

(59) Yin, Y.; Alivisatos, A. P. Colloidal Nanocrystal Synthesis and the Organic–Inorganic Interface. *Nature* **2005**, *437*, 664–670.

(60) Testa-Anta, M.; Rodríguez-González, B.; Salgueiriño, V. Partial FeO–Fe_3O_4 Phase Transition Along the <111> Direction of the Cubic Crystalline Structure in Iron Oxide Nanocrystals. *Part. Part. Syst. Charact.* **2019**, *36* (11), 1–7.

(61) Santos-Carballal, D.; Roldan, A.; Grau-Crespo, R.; de Leeuw, N. H. A DFT Study of the Structures, Stabilities and Redox Behaviour of the Major Surfaces of Magnetite Fe_3O_4. *Phys. Chem. Chem. Phys.* **2014**, *16* (39), 21082–21097.

(62) Kim, D.; Lee, N.; Park, M.; Kim, B. H.; An, K.; Hyeon, T. Synthesis of Uniform Ferrimagnetic Magnetite Nanocubes. *J. Am. Chem. Soc.* **2009**, *131*, 454–455.

(63) Marqusee, J. A.; Ross, J. Theory of Ostwald Ripening: Competitive Growth and Its Dependence on Volume Fraction. *J. Chem. Phys.* **1984**, *80* (1), 536–543.

(64) Kirchner, H. O. K. Coarsening of Grain-Boundary Precipitates. *Metall. Trans.* **1971**, *2* (10), 2861–2864.

(65) Huang, F.; Zhang, H.; Banfield, J. F. Two-Stage Crystal-Growth Kinetics Observed during Hydrothermal Coarsening of Nanocrystalline ZnS. *Nano Lett.* **2003**, *3* (3), 373–378.

(66) Leszczyński, B.; Hadjipanayis, G. C.; El-gendy, A. A.; Za, K.; Zbigniew, Ś.; Musia, A.; Jarek, M.; Jurga, S.; Skumiel, A. The Influence of Oxidation Process on Exchange Bias in Egg-Shaped FeO/Fe$_3$O$_4$ Core/Shell Nanoparticles. *J. Magn. Magn. Mater.* **2016**, *416*, 269–274.

(67) Verwey, E. J. W. Electronic Conduction of Magnetite (Fe$_3$O$_4$) and Its Transition Point at Low Temperatures. *Nature* **1939**, *144* (3642), 327–328.

SYNOPSIS (Word Style "SN_Synopsis_TOC")

.